Two-Stage Anomaly Detection in Super High-Rise Fire Sensor Networks Using Low-Rank Completion and RV-GAN

Congyue Qi[1], Qinghua Tan[1], Ji Liao[2], Lijun Yuan[2*]
[1]School of Civil Engineering, Tsinghua University, Beijing 100084, China
[2]The Third Construction Co., Ltd of China Construction Third Engineering Bureau, Wuhan 437000, China
E-mail: cscecqcy@vip.qq.com, qinghuatan@gxu.edu.cn, 517943238@qq.com, 15623783703@163.com
[*]Corresponding author

Keywords: super high-rise building, fire monitoring, sensor data anomaly, low-rank completion, generative adversarial network

Received: September 3, 2025

With the increasing intelligence of fire protection systems in super high-rise buildings, fire monitoring schemes based on sensor networks have raised higher requirements in terms of perception accuracy and response efficiency. However, complex spatial environments and instability in the performance of sensing equipment often led to anomalies such as missing, drifting, and distorted data collection. To address these challenges, this study develops a two-stage anomaly detection framework based on low-rank completion and generative adversarial learning. In the first stage, the Correlation-Regularized Schatten-p Precompletion (CRSP-Pre) model leverages feature correlations and low-rank constraints to structurally repair abnormal or missing samples. In the second stage, a Residual-Variational Generative Adversarial Network (RV-GAN) is designed to capture high-order and composite anomalies through variational generation and residual discrimination mechanisms. Experimental results show that when the data missing rate reaches 50%, the mean absolute error (MAE) and structural similarity index (SSIM) are 0.131 and 0.671, respectively-representing improvements of approximately 15% and 12% over conventional completion and single-stage detection methods. When the number of nodes is 40, the false alarm rate of the proposed method is 5.4%, the model parameter size is 7.8M, and the inference time is 22.4 ms. The results show that the method has good robustness and engineering adaptability, effectively enhancing the processing capability and response reliability of fire monitoring systems for abnormal data. It provides a technical path for intelligent management of sensing data in complex building environments.

Povzetek: Študija razvije metodo za bolj zanesljivo zaznavanje in popravljanje napak v senzorskih podatkih požarnega nadzora v visokih stavbah.

1 Introduction

With the continuous improvement of intelligence and automation management in super high-rise buildings, fire monitoring systems based on multi-source perception are becoming a key support for ensuring the safe operation of buildings [1]. Fire monitoring sensors are widely deployed inside buildings to achieve real-time collection and early warning response of key indicators such as smoke, temperature, and carbon monoxide concentration, effectively supporting intelligent linkage tasks such as fire detection, evacuation control, and disaster disposal [2, 3]. However, under the influence of multiple factors such as complex spatial layout, high-frequency data flow, and unstable communication, sensor systems are prone to issues such as data drift, loss, or abnormal mutations, which in turn affect the stability and accuracy of judgment of the overall fire monitoring system [4, 5]. To address these challenges, current research focuses on using computer intelligent algorithms to precisely identify and efficiently repair abnormal sensor data, thereby enhancing the robustness and perception reliability of the monitoring system. In this context, numerous scholars have conducted a series of studies on the construction and model optimization of algorithms for detecting sensor data anomalies. Gursel et al. proposed a generative adversarial anomaly detection model incorporating physical information to address anomalies caused by sensor errors or human errors in nuclear power plants. This method utilized the known physical characteristics of the system to constrain sensor output, effectively improving the credibility and accuracy of anomaly detection, and performing better in anomaly identification of sensor and manual monitoring data [6]. Wang et al. proposed a distributed detection method based on adaptive grouping to address issues such as neglecting inter-node correlation and high communication overhead in wireless sensor network anomaly detection. This scheme constructed node groups through graph theory analysis, performed local detection combined with edge cloud architecture, and introduced a

consistency evaluation mechanism to enhance detection reliability [7]. Ahmad et al. proposed a lightweight unsupervised anomaly detection method combining continuous wavelet transform and support vector clustering to address issues such as high computational complexity and lack of data annotation in real-time sensor data, demonstrating good adaptability to data streams [8]. Su et al. constructed an anomaly detection model integrating graph attention mechanism and temporal convolution to address the challenges of complex inter-time series correlation and scarce abnormal samples in wireless sensor networks. This method jointly modeled the potential relationships between feature dimensions and time dimensions, effectively alleviating the problem of extreme imbalance between positive and negative samples [9].

Based on this, some scholars have expanded their research perspectives to the optimization of IoT architecture and cross-domain anomaly detection, further enhancing the adaptability and intelligence of sensor data processing in complex scenarios. Allka et al. addressed the issue of data reliability brought by low-cost IoT sensors in air quality monitoring networks, proposing a cyclic autoencoder anomaly detection structure that integrates temporal and spatial correlations. This method involved not only the temporal characteristics of the sensors themselves but also the spatial relationships between adjacent devices in the detection network for reconstruction [10]. Pan et al. tackled the problems of input data distribution differences and sensor redundancy dependencies in multivariate time series anomaly detection, introducing a self-attention network method that incorporates a dual masking mechanism. This method enhanced the adaptability of the predictor to abnormal inputs through block-level masking and introduces a maximum masking strategy to reduce misleading effects from unrelated sensors [11]. Gutierrez-Rojas et al. constructed a multi-module anomaly detection model for industrial IoT systems supported by wireless sensors. This structure integrated three key processes: data collection, fusion, and decision-making, and introduced interpretable artificial intelligence algorithms to enhance anomaly analysis capabilities [12]. Prabowo et al. designed an automatically operable sensor anomaly detection system to address the issue of manual processing required for sensor data anomalies in IoT platforms. This system was integrated into a general IoT architecture, enabling intelligent anomaly elimination from data collection to preprocessing stages [13]. To position the proposed framework within existing research. Table 1 presents a summary of key related works covering diverse sensor-network anomaly detection methods.

Table 1: Summary of representative related works.

Reference	Task/Domain	Method Category	Core Idea and Contribution
Gursel et al. [6]	Anomaly detection in reactor sensor data	Physics-informed GAN model	Integrates human-error and sensor-fault modeling within a unified system-level anomaly detection framework.
Wang et al. [7]	Anomaly detection in wireless sensor networks (WSN)	Correlation-aware distributed detection	Utilizes inter-node correlation for group-based distributed detection, enhancing reliability in WSNs.
Ahmad et al. [8]	Lightweight anomaly detection in sensors	Continuous wavelet transform + vector clustering	Employs efficient feature extraction and clustering for resource-constrained sensor devices.
Su et al. [9]	WSN data-stream anomaly detection	Joint optimization of GATv2 and TCN	Combines spatial topology learning (GATv2) and temporal modeling (TCN) for joint spatiotemporal representation.
Allka et al. [10]	IoT-based sensor-network anomaly detection	Recurrent autoencoder (RAE)	Leverages spatiotemporal correlations through sequence reconstruction, suitable for large-scale IoT platforms.
Pan et al. [11]	Multivariate time-series anomaly detection	Dual-mask self-attention network (DUMA)	Applies block-masking and max-masking strategies to enhance adaptability to abnormal inputs.
Gutierrez-Rojas et al. [12]	Anomaly detection in WSN-enabled cyber-physical systems (CPS)	Interpretable multi-module framework	Integrates data collection, fusion, and decision stages, emphasizing interpretability and modularity.
Prabowo et al. [13]	Environmental-sensor anomaly detection in IoT platforms	End-to-end anomaly-elimination pipeline	Proposes a cloud–edge pipeline for large-scale IoT anomaly detection with high deployment practicality.

In summary, under the complex monitoring environment of super high-rise buildings, sensor data still generally faces bottleneck issues such as diverse types of anomalies, low accuracy in anomaly detection, and unstable data recovery. To address this, a two-stage integrated method that combines low-rank data completion and deep generative detection is designed, aiming to enhance the overall performance of fire sensor

systems in anomaly perception and error recovery. Specifically, it includes two innovations: Firstly, the CRSP-Pre is proposed to achieve structured recovery and information reconstruction of anomalous samples. Secondly, the RV-GAN is constructed to achieve precise identification of high-order anomalies, enhancing the model's responsiveness and practical deployment adaptability in extreme event monitoring.

Accordingly, the core research question of this study is: Can a two-stage approach, which seamlessly combines low-rank completion and generative adversarial learning, substantially enhance anomaly-detection performance under conditions of high missing rates, all the while preserving computational efficiency? This question forms the foundation of the methodological design described in Section 2.

2 Methods and materials

2.1 Anomaly preprocessing based on feature correlation and low-rank completion

In the intelligent fire protection system of super high-rise buildings, sensor data often experiences missing values and noise due to channel interference or node failures, affecting the stability of subsequent anomaly detection [14]. To address this, a correlation-driven data completion model, CRSP-Pre, is proposed. It combines spatiotemporal correlation modeling and weighted low-rank constraints to achieve high-quality restoration of fire monitoring data and preliminary screening of outliers. The overall process is illustrated in Figure 1.

As shown in Figure 1, CRSP-Pre takes raw fire monitoring data as input. In the first stage, it completes preliminary completion by measuring the correlation between historical and neighboring sensors using the Pearson Correlation Coefficient (PCC). In the second stage, it reconstructs the underlying low-rank structure through joint constraints of the weight matrix and Schatten-p norm, enhancing the perception ability for outliers under sparse optimization. During the optimization process, the Alternating Direction Method of Multipliers (ADMM) algorithm is used for iterative solving, achieving precise recovery of missing values and potential outliers, providing reliable data support for subsequent detection.

The core objective of the first stage is to perform preliminary interpolation and completion of missing data based on the correlation between sensors, as illustrated in Figure 2.

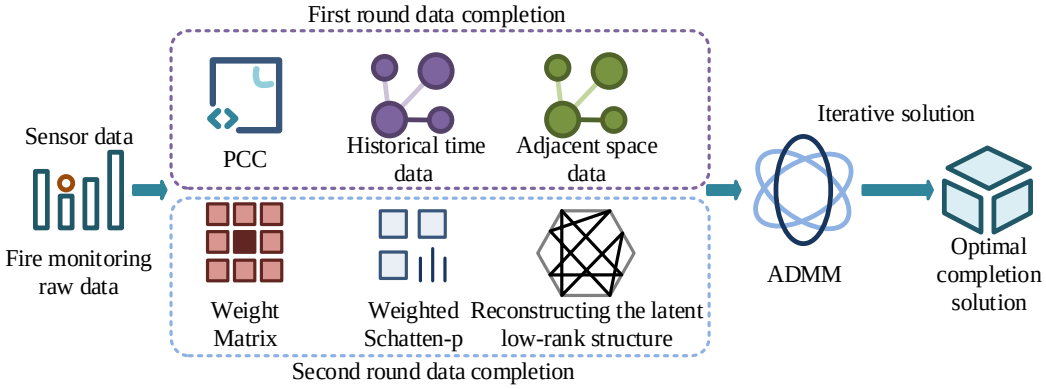

Figure 1: CRSP-Pre model structure for anomaly repair.

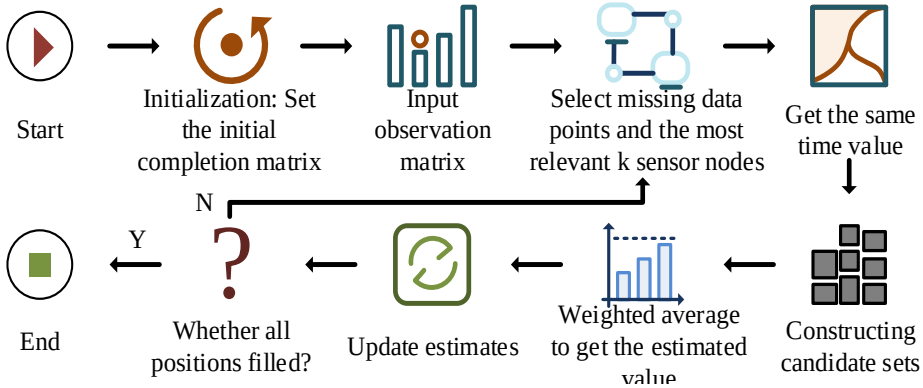

Figure 2: PCC-based initial completion algorithm process.

As shown in Figure 2, with the observation matrix X as input, for each missing data point, the most relevant k sensor nodes are selected in turn to obtain the values at the same time, forming a candidate set, and the estimated value is obtained through weighted average. The completion process is iteratively applied to all missing points until all positions are filled or the maximum iteration count is reached. First, let the original

data matrix be denoted as X, and the mask matrix as $M \in \{0,1\}^{m\times n}$, where $M_{ij}=1$ indicates that the corresponding item x_{ij} has an observed value. Otherwise, it equals 0, indicating a missing value. The initial completion matrix is denoted as $\hat{X}^{(0)}=X$. For each missing item x_{tj}, the correlation with other sensor nodes is calculated using PCC. The correlation coefficient between node i and node j is denoted as equation (1).

$$\rho_{ij}=\frac{\sum_{t=1}^{m}(x_{ti}-\mu_i)(x_{tj}-\mu_j)}{\sqrt{\sum_{t=1}^{m}(x_{ti}-\mu_i)^2}\cdot\sqrt{\sum_{t=1}^{m}(x_{tj}-\mu_j)^2}} \tag{1}$$

In equation (1), μ_i and μ_j represent the mean values of node i and node j in the time dimension. ρ_{ij} denotes the PCC between node i and node j in the historical time series. Based on the absolute value of ρ_{ij}, the most relevant sensor set is constructed for each target node j. Then, a subset of nodes with valid observations at time t is selected, and an estimation expression for missing values is defined accordingly, as shown in equation (2).

$$\hat{x}_{tj}^{(1)}=\frac{\sum_{i\in N_k^+(j)}|\rho_{ij}|\cdot x_{ti}}{\sum_{i\in N_k^+(j)}|\rho_{ij}|} \tag{2}$$

In equation (2), $\hat{x}_{tj}^{(1)}$ represents the estimation result of missing value x_{tj} during the initial completion stage. If sufficient neighbor node observations are missing at some points, a historical adjacent time slice backtracking mechanism can be introduced as a supplement. After completing the first stage of estimation and completion process, the preliminary filled matrix $\hat{X}^{(1)}=PCC-Interpolate(X,M,k)$ is obtained. This matrix will be further fed into the low-rank completion framework in the second stage to achieve structural anomaly identification and optimized recovery.

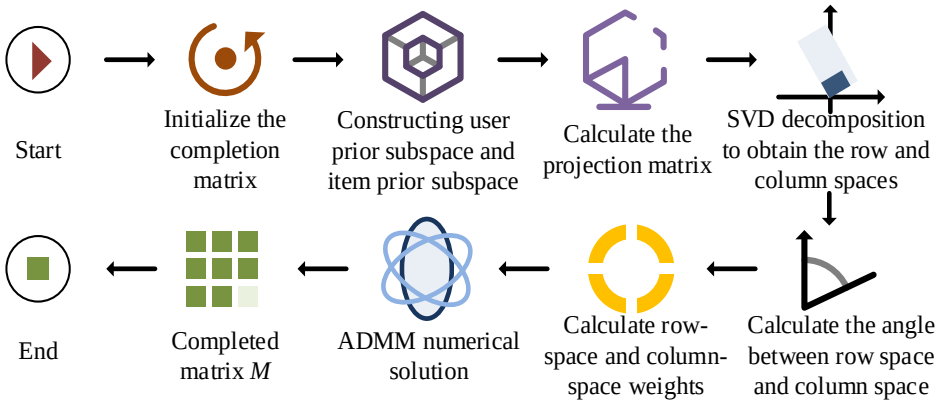

Figure 3: Weighted Schatten-p norm-based data refinement process.

To enhance the structural consistency and anomaly discriminability of the completed matrix, the weighted Schatten-p (0<p<1) norm is introduced in the second stage as a closer alternative to the matrix rank. It alleviates the excessive contraction of large singular values and better preserves the principal subspace under high missing rates. Although the non-convex form increases the optimization complexity, it can be effectively solved using ADMM with iteratively reweighted singular value thresholding (IRLS), thus achieving a good balance between reconstruction accuracy and computational efficiency [15]. The overall process of the second stage is shown in Figure 3.

In Figure 3, the completion matrix is first projected into predefined user subspace and sensor subspace. Subsequently, the angle between the two subspaces is calculated and the weight coefficient is constructed. On this basis, the weighted Schatten-p norm is introduced to construct the low-rank optimization objective function, and the numerical solution is obtained with the help of ADMM. Finally, the optimized completion result is output. Assuming the output matrix of the first stage is Z, the optimization objective is to find a low-rank sparse matrix M to minimize its weighted Schatten-p norm, as shown in equation (3).

$$\|M\|_{S_p}^{p}=\sum_{i'=1}^{\min(m,n)}\sigma_{i'}^{p} \tag{3}$$

In equation (3), σ_i is the i' th singular value of matrix M, and $p\in(0,1]$ controls the strength of regular sparsity. To incorporate structural guidance information, the study constructs a prior user subspace $\hat{U}_r$ and a sensor subspace $\hat{V}_r$, and measures the angle between the current subspace and the prior subspace. To construct the prior subspaces U_0 and V_0, the coarsely completed matrix X_0 obtained via PCC–Interpolate is decomposed using truncated SVD to extract the dominant column and row subspaces, representing user and sensor priors, respectively. These subspaces capture the major spatial–temporal correlation patterns in the observed data. In

cases without prior knowledge, U_0 and V_0 are initialized from random orthogonal bases of the same rank. The subspace angles are then calculated as shown in equation (4).

$$\theta_u = \arccos\left(\frac{\langle U, \hat{U}_r \rangle}{\|U\|_F \cdot \|\hat{U}_r\|_F}\right), \theta_v = \arccos\left(\frac{\langle V, \hat{V}_r \rangle}{\|V\|_F \cdot \|\hat{V}_r\|_F}\right) \quad (4)$$

In equation (4), U and V represent the left and right singular vector matrices obtained after performing singular value decomposition on the matrix. M denotes the Frobenius inner product, and $\langle \cdot, \cdot \rangle$ denotes the Frobenius norm. Subsequently, the angle value is converted into a directional weight through a mapping function, as shown in Equation (5).

$$w_u = f(\theta_u), \quad w_v = f(\theta_v) \quad (5)$$

In equation (5), θ_u and θ_v represent the angles between the current subspace and the user's prior subspace, as well as the sensor's prior subspace, respectively. Ultimately, a Schatten-p norm minimization model with bidirectional weight factors is constructed, as shown in equation (6).

$$\begin{aligned} &\min_{M} \quad \lambda_u w_u \|M\|_{S_p} + \lambda_v w_v \|M\|_{S_p} \\ &s.t. M_{ij} = Z_{ij}, \forall (i'', j) \in \Omega \end{aligned} \quad (6)$$

In equation (6), Z_{ij} represents the corresponding observed value in the initial completion matrix (output matrix of the first stage). Ω is the set of observed data positions. λ_u and λ_v are regularization strength adjustment factors in two directions. (i'', j) denotes the position corresponding to the i'' th time record and the j th sensor node in the data matrix.

Due to the presence of a non-convex Schatten-p norm term in the objective function and projection constraints, ADMM is introduced for optimization and solution. This algorithm equivalently transforms the problem into a function with Lagrange multipliers in the following form by introducing auxiliary variables, as shown in Equation (7).

$$L_\eta(M, Y, A) = f(M) + g(Y) + \langle A, M - Y \rangle + \frac{\eta}{2}\|M - Y\|_F^2 \quad (7)$$

In equation (7), η is the penalty factor of ADMM. A is the multiplier matrix. The algorithm gradually converges to a low-rank matrix M^* by alternately minimizing each variable and updating the multiplier. To ensure stability and convergence of the optimization process, the ADMM iteration adopts an adaptive penalty parameter and standard stopping criteria. The penalty parameter η is initialized to 0.1 and updated by a factor of 1.5 every 20 iterations. The optimization terminates when both primal and dual residuals fall below 10−4, or when 300 iterations are reached. The penalty parameter η is initialized to 0.1 and adaptively updated by a factor of 1.5 every 20 iterations. The selection and sensitivity of η are further analyzed in Section 3.1, where the parameter range 0.1-1.0 was tested to confirm convergence stability and accuracy.

2.2 High-order anomaly detection method based on deep generative models

After completing the preprocessing of sensor data based on feature correlation and low-rank structure constraints, abnormal information can be repaired and filled to a certain extent. However, in the complex spatial environment of super high-rise buildings, sensor data fluctuations induced by fires often exhibit nonlinear mutations or multidimensional covariant patterns [16, 17]. To this end, the study proposes a deep Residual Variational Generative Adversarial Network (RV-GAN), which achieves precise identification and differentiation of high-order anomalies by jointly modeling the potential spatial distribution and data generation discrimination mechanism. Its structure is shown in Figure 4.

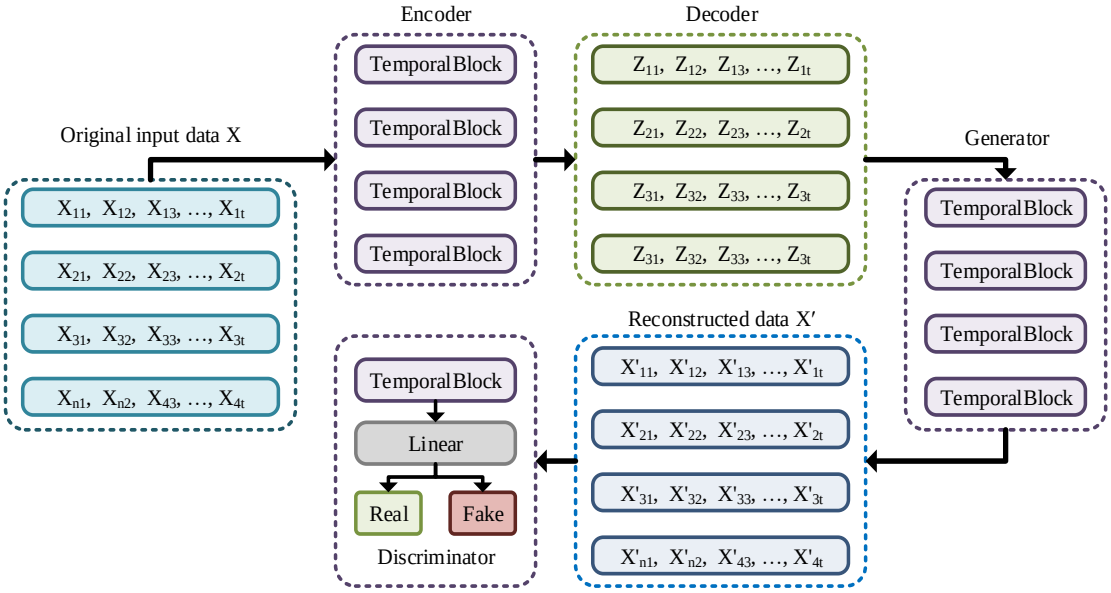

Figure 4: RV-GAN model architecture for anomaly detection.

As shown in Figure 4, the RV-GAN model comprises four main modules: Encoder, Decoder, Generator, and Discriminator, all of which are embedded with temporal convolutional modules to extract multi-scale dynamic features. Specifically, the Encoder maps time series samples to latent variable space, the Decoder reconstructs input data based on the reparameterization strategy of the Variational Auto-Encoder (VAE), the Generator further fits high-fidelity pseudo-samples through a residual convolutional structure, and the Discriminator combines the Wasserstein distance and a linear projection classifier to determine whether the samples originate from the original data distribution, thus achieving robust discrimination of potential anomalies.

To further clarify the network design, the generator in RV-GAN consists of five convolutional blocks and two transposed convolution layers for upsampling. Each convolution uses a 3×3 kernel, stride 1, and LeakyReLU activation (α=0.2), with Tanh used in the output layer to constrain reconstruction values. Batch normalization is applied after each convolution to stabilize training. The residual convolution module contains three residual units with 3×3 kernels and skip connections to enhance feature preservation and gradient flow. The generator and decoder are independently parameterized to prevent gradient interference, while the discriminator follows a PatchGAN-style architecture with progressively increasing channel depths (64–128–256–512).

To enhance the ability to identify high-order potential anomalies, the RV-GAN model adopts a structure that combines deep variational encoding mechanisms with adversarial learning strategies to achieve implicit modeling and generative discrimination of anomalous samples. The input multi-dimensional sensor time series are denoted as $S=[s_1,s_2,...,s_T]$, where T denotes the length of the sampling time window and D denotes the number of sensors or dimensions. The encoder module, based on a temporal convolutional network, encodes the original sequence into distribution parameters in the latent space, including the mean vector μ and the logarithmic variance vector $\log\sigma^2$, with the mapping relationship expressed as Equation (8).

$$\mu,\log\sigma^2=G_e(S) \tag{8}$$

In equation (8), $G_e(\cdot)$ represents the encoder network function, which outputs parameters used to construct the distribution of latent variables. Subsequently, based on the reparameterization technique proposed in VAE, the latent vector z is sampled from the Gaussian distribution using the sampling method shown in equation (9).

$$z=\mu+\sigma\otimes\grave{o},\quad \grave{o}\sim N(0,I) \tag{9}$$

In equation (9), $\otimes$ represents the element-wise multiplication operation, $\grave{o}$ is the standard normal distribution noise vector, $\sigma=\exp(0.5\cdot\log\sigma^2)$ represents the standard deviation vector, ensuring the differentiability of the sampling. The latent variable z is fed into the decoder $G_d(\cdot)$ and the residual generator $G_r(\cdot)$ to obtain the reconstructed sample and the generated sample, respectively, as expressed in equation (10).

$$\hat{S}=G_d(z),\quad \bar{S}=G_r(z) \tag{10}$$

In equation (10), $\hat{S}$ and $\bar{S}$ represent the reconstructed sample and generated sample, respectively. The model introduces a discriminator $D(\cdot)$, using the Wasserstein distance as the optimization objective between generation and discrimination. The overall training objective function consists of three parts. The first is the reconstruction loss, which is composed of the VAE reconstruction error term and the KL divergence term, as shown in equation (11) [18].

$$L_{VAE}=E_{q(z|S)}[\left\|S-\hat{S}\right\|_2^2]+\beta KL(q(z|S)\|p(z)) \tag{11}$$

In equation (11), the first term represents the mean squared reconstruction error, while the second term represents the KL divergence between the latent variable distribution $q(z|S)$ and the standard normal distribution $p(z)$, serving as a regularization constraint. The balance between these two components is controlled by a weighting coefficient β, which follows the design of β-VAE. In this study, β is empirically set to 0.5 to ensure a proper trade-off between reconstruction fidelity and latent compactness. Sensitivity analysis confirms that the performance is stable for $\beta\in$[0.3, 0.7], and dynamic scheduling of β is unnecessary. Secondly, the adversarial loss based on the Wasserstein distance is introduced to train the game relationship between the generator and the discriminator, which is defined as equation (12) [19, 20].

$$L_{WGAN}=E_{\bar{S}\sim G_r(z)}[D(\bar{S})]-E_{S\sim P_r}[D(S)]+\lambda\cdot E_{\hat{S}\sim P_{\hat{S}}}[(\left\|\nabla_{\hat{S}}D(\hat{S})\right\|_2-1)^2] \tag{12}$$

In equation (12), P_r represents the true sample distribution, and $P_{\hat{S}}$ is a mixed distribution obtained by linear interpolation between the true samples and the generated samples. λ denotes the gradient penalty coefficient, ensuring that the discriminator satisfies the Lipschitz condition. The gradient penalty term in equation (12) is implemented with reference to WGAN-GP. The gradient is calculated at the linear interpolation points between the real samples and the generated samples, see equation (13).

$$\hat{S}=\grave{o}S+(1-\grave{o})\tilde{S},\grave{o}\sim U(0,1) \tag{13}$$

As shown in Equation (13), during training, the discriminator and generator are updated alternately with a ratio of 5:1, and the Adam optimizer (learning rates 1e-4 and 2e-4) is used respectively. This configuration exhibits stable convergence characteristics in

experiments and avoids the problems of gradient explosion and mode collapse.

Ultimately, the joint loss function of RV-GAN is the weighted sum of the above two parts. During the training process, model parameters are iteratively optimized through backpropagation and gradient clipping strategies to ensure stable convergence and discriminative ability under different abnormal patterns. To visually demonstrate the specific execution logic of RV-GAN in the task of anomaly detection for super high-rise building fire sensor data, the process framework diagram is shown in Figure 5.

In Figure 5, the left side represents the training path, where normal data are encoded to extract latent vectors, and the Wasserstein Generative Adversarial Network (WGAN) composed of a generator and a discriminator accomplishes the adversarial optimization. The right side represents the testing path, where mixed data is input, decoded, and reconstructed by a Variational Autoencoder (VAE). The system determines the degree of abnormality based on the reconstruction error and the discrimination results. To comprehensively describe the complete process of the research in the task of anomaly detection for fire sensors in super high-rise buildings, the research integrates feature correlation modeling, low-rank completion, and generative anomaly recognition in an end-to-end manner, constructing a two-stage scoring process as shown in Figure 6.

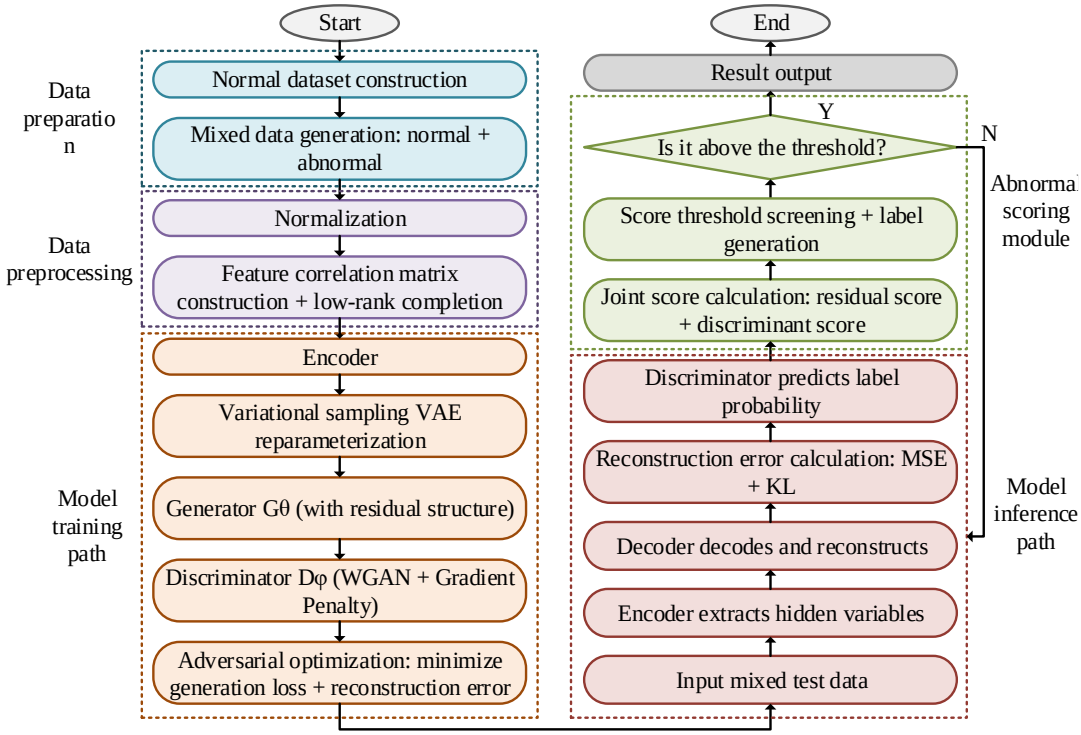

Figure 5: Workflow of RV-GAN in fire sensor anomaly detection task.

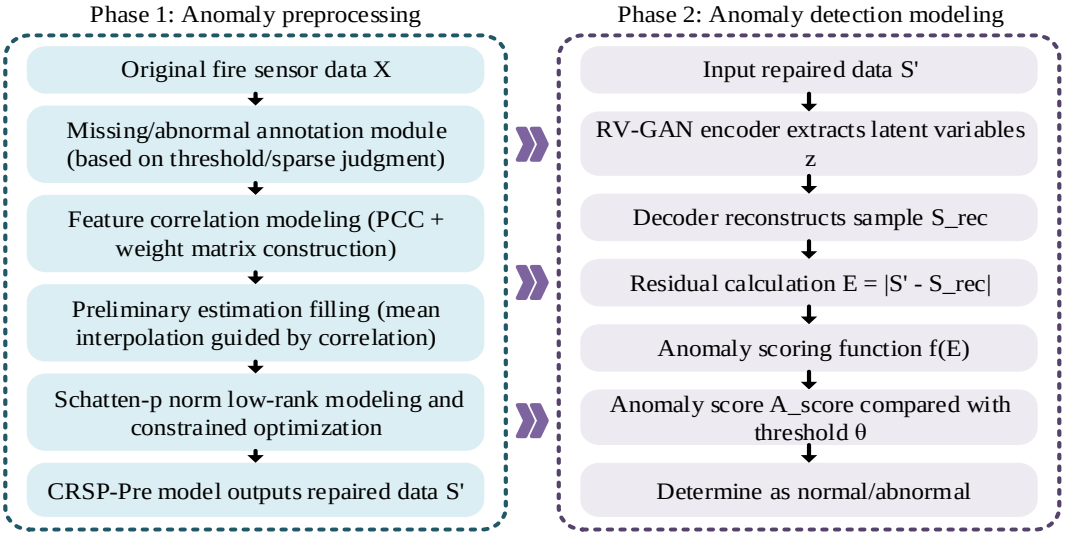

Figure 6: Two-stage anomaly detection process for super high-rise fire sensor data.

As illustrated in Figure 6, the overall workflow operates through two consecutive and cooperative stages. In the first stage, the CRSP-Pre module performs data annotation, correlation-based interpolation, and low-rank reconstruction to repair missing or abnormal sensor readings, producing a structurally complete dataset. In the second stage, the RV-GAN module receives the repaired data and conducts high-order anomaly recognition through feature encoding, sample reconstruction, and residual scoring to determine anomaly levels. Together, the two stages form an integrated framework in which the first stage ensures data completeness, while the second provides accurate semantic discrimination, enabling reliable and robust anomaly detection in super high-rise fire monitoring systems.

3 Results

3.1 Performance evaluation of CRSP-Pre abnormal data repair

The study constructed an experimental platform for anomaly detection in sensor data from super high-rise buildings, based on Python 3.10 and PyTorch 2.0.1. The operating environment included an Intel Core i9-12900K processor, 128GB of memory, and an Ubuntu 20.04 operating system. Model training and inference were completed on an NVIDIA RTX 3090 GPU. The experiment utilized the IBRL wireless sensor dataset to evaluate the robustness of the model under standard environmental perception and complex distribution scenarios. To ensure reproducibility and prevent data leakage, both datasets were divided into training, validation, and testing subsets using a time-based non-overlapping split. Specifically, the first 70% of the temporal sequence was used for model training, the following 15% for validation, and the remaining 15% for testing. To assess the stability and convergence efficiency of the proposed model under different parameter configurations, the Schatten-p order p, regularization weight combination (λ_u, λ_v), and ADMM optimization penalty parameter η were set as core variables for a three-factor combination test. A sparse observation matrix with a missing rate of 15% was constructed, and the parameters in the initial completion stage were kept fixed, focusing on exploring the impact of sparse matrix optimization in the second stage on final performance. Each parameter combination was repeated five times, and the results are averaged. The results are presented in Table 2.

From Table 2, as the p value increased from 0.1 to 1.0, the performance of the model in terms of mean squared error and relative error continued to improve. Higher orders contributed to enhancing the low-rank representation ability of matrix completion. When the regularization weight (λ_u, λ_v) was set at a moderate level, the model achieved a better balance between accuracy and convergence. An overly small regularization coefficient limited the sparse structure's ability to model anomalies, while an excessively large one tended to lead to overfitting. Taking a larger value for the penalty parameter η could accelerate the iterative convergence process while ensuring accuracy. The combination of p =1.0, (λ_u, λ_v) =0.5, and η =10.0 was ultimately determined as the optimal parameter configuration for the model, which was used for unified scheduling and execution of each module in subsequent experiments.

To verify the model's ability to recover sensor data under high missing rates and maintain structural fidelity, the missing rate range was set from 10% to 50%, examining the model's reconstruction performance under different degrees of data sparsity. Three typical models in the current field were selected for comparison, including Spatio-Temporal Attention Embedded Autoencoder (STAEA), Graph Convolutional Completion Network (GCCN), and Spatio-Temporal Correlated Recurrent Network (STCRNet), representing attention mechanisms, graph modeling, and temporal modeling structures, respectively. The comparative evaluation metrics used were Mean Absolute Error (MAE) and Structural Similarity Index (SSIM). Each experiment was independently repeated five times with different random initializations, and the reported results represent the mean ± standard deviation to ensure statistical reliability. The corresponding experimental results are shown in Figure 7.

Table 2: Parameter sensitivity test results.

Schatten-p order p	Regularization weights (λ_u, λ_v)	ADMM penalty parameter η	Mean Squared Error ↓	Mean Absolute Relative Error (%) ↓	Convergence rounds ↓	Average runtime (s) ↓
0.1	(0.1, 0.1)	0.1	0.1145	8.91	36	4.82
0.1	(0.5, 0.5)	1.0	0.0932	6.84	28	3.75
0.1	(1.0, 1.0)	10	0.0879	6.29	25	3.51
0.5	(0.1, 0.1)	1.0	0.0723	5.32	24	3.11
0.5	(0.5, 0.5)	1.0	0.0649	4.88	27	3.46
0.5	(0.5, 0.5)	10	0.0622	4.70	22	3.02
1	(0.1, 0.1)	1.0	0.0578	4.51	21	2.97
1	(0.5, 0.5)	1.0	0.0547	4.33	19	2.91
1	(0.5, 0.5)	10	0.0535	4.29	16	2.38

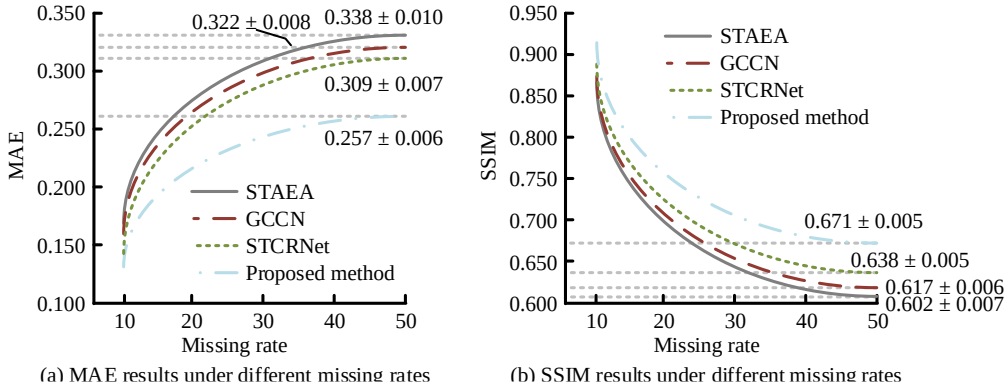

(a) MAE results under different missing rates (b) SSIM results under different missing rates

Figure 7: Model performance test under different missing rates. (Values represent the mean ± standard deviation (SD) over five independent runs.)

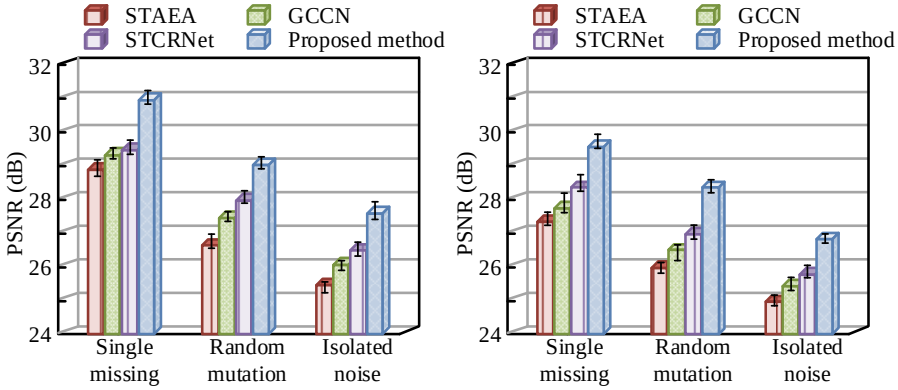

(a) PSNR comparison under point anomaly conditions (b) PSNR comparison under clustered anomaly conditions

Figure 8: Comparison of recovery performance under different anomaly types.

In Figure 7(a), when the missing rate was 10%, the MAE of STAEA, GCCN, STCRNet, and the proposed method were 0.167 ± 0.006, 0.155 ± 0.005, 0.143 ± 0.004, and 0.131 ± 0.004. At a 50% missing rate, they increased to 0.338 ± 0.010, 0.322 ± 0.008, 0.309 ± 0.007, and 0.257 ± 0.006. In Figure 7(b), when the missing rate was 10%, the SSIM of the four methods were 0.861 ± 0.005, 0.873 ± 0.006, 0.889 ± 0.005, and 0.907 ± 0.004. When the missing rate increased to 50%, they decreased to 0.602 ± 0.007, 0.617 ± 0.006, 0.638 ± 0.005, and 0.671 ± 0.005. The proposed method in this study combined the encoder and multi-scale residual reconstruction module during the modeling process, effectively preserving the spatiotemporal structural information of the data. In contrast, although STAEA introduced a spatiotemporal attention mechanism, it ignored the continuous aggregation of neighboring dependency information. Although GCCN and STCRNet could model graph structures or cyclic relationships, they suffered from severe breaks in the information propagation chain under high missing rates, making it difficult to support stable reconstruction. Therefore, their overall performance was slightly inferior.

Subsequently, the abnormal data in the test set were divided into two categories. Point-like anomalies simulated isolated sensor failures, encompassing three types of perturbations: single-point missing, single-point offset, and single-point noise. Cluster-like anomalies simulated dense collection anomalies, covering three typical scenarios: local missing, regional outbreak, and block drift. Under each abnormal condition, the peak signal-to-noise ratio (PSNR) and reconstruction stability index (RSI) of the model output were measured, and the results are shown in Figure 8.

In Figure 8(a), under three types of point-like anomalies, the PSNR of the proposed model under single-point missing, random perturbation, and outlier noise conditions reached 30.81 dB, 28.92 dB, and 27.42 dB, all of which were superior to the comparative model. In Figure 8(b), under three types of cluster-like anomalies, the PSNR of the proposed model under abrupt drift, continuous distortion, and local outbreak scenarios were 29.36 dB, 28.02 dB, and 26.81 dB. Comparative methods were limited by convolutional receptive fields or temporal dependency structures, making it difficult to accurately capture spatial coupling and cross-node abrupt changes, leading to a decrease in reconstruction accuracy.

3.2 Performance evaluation of anomaly detection model RV-GAN

The experiment was conducted based on the Smart Fire Detection Sensors dataset provided by Stanford University. This dataset was collected from multiple sensors in high-rise building environments, including smoke, temperature, infrared heat, and carbon monoxide sensors, which includes data from normal operation, false alarms, disturbance anomalies, and actual fire events. A time-based sequential split was applied to preserve the temporal continuity of fire evolution. The first 70% of the chronological sequence was used for training, the following 15% for validation, and the remaining 15% for testing. To avoid spatial leakage, the split was performed independently for each sensor node group, ensuring that test samples originated from future time windows not seen during training. Ablation experiments were designed to test the removal of the Encoder, VAE, and Residual Generator (RG) respectively. The Anomaly Detection Accuracy (ADA) and Structural Similarity Index (SSIM) under different structural configurations were evaluated to analyze the impact of each submodule on the overall detection capability. The experimental results are shown in Figure 9.

In Figure 9(a), when the number of iterations reached 500, the ADA of removing the Encoder, VAE module, and RG were 87.2, 86.5, and 89.5, while the complete model achieved an ADA of 92.7. In Figure 9(b), under the same conditions, the SSIM scores were 0.870, 0.863, and 0.888, with the complete model scoring 0.902. The absence of the Encoder led to insufficient expression of latent variable distributions, affecting the overall reconstruction quality. The lack of regularization optimization capability in VAE reduced the generalization ability of anomaly modeling. As an important module for completing high-frequency information, the removal of RG directly led to incomplete anomaly expression.

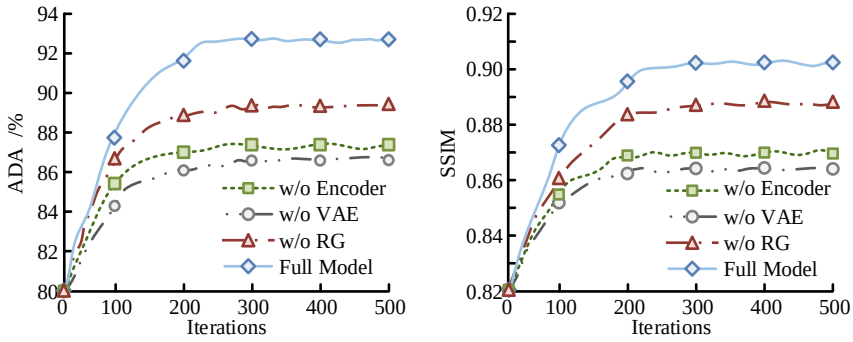

(a) ADA results under different iterations (b) SSIM results under different iterations

Figure 9: Ablation experiment results.

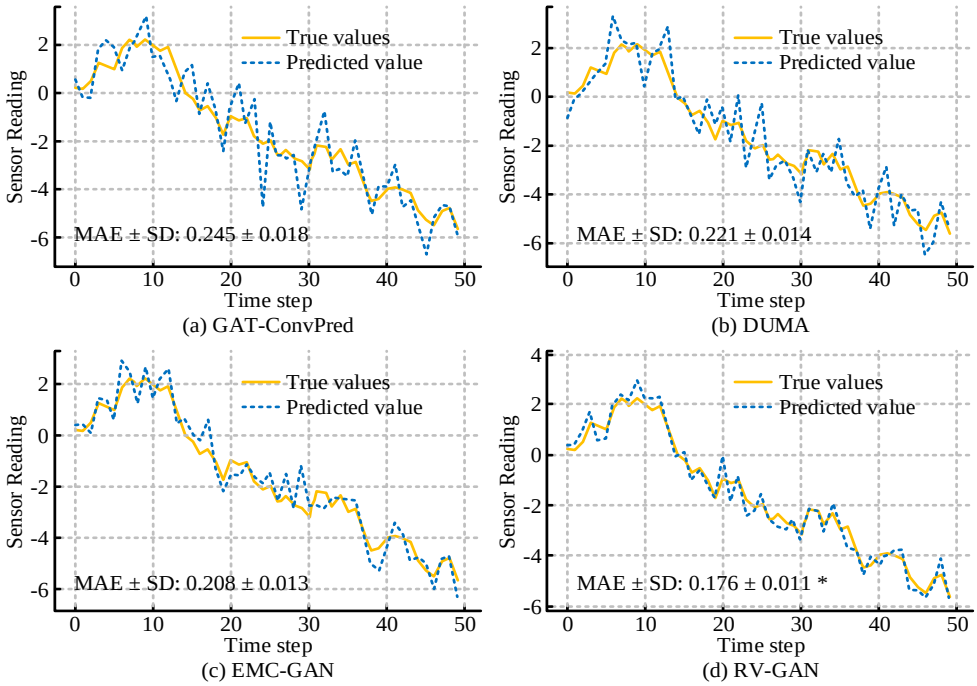

Figure 10: Prediction results on fire sensor data. Comparison of predicted and true sensor readings using four models: (a) GAT-ConvPred, (b) DUMA, (c) EMC-GAN, and (d) RV-GAN. Statistical annotations (MAE ± SD) are calculated over five independent runs. Asterisks (*) indicate statistically significant differences ($p < 0.05$, paired t-test) compared with the baseline model (EMC-GAN).

The Graph Attention-based Convolutional Predictor (GAT-ConvPred), Dual-Mask Self-Attention Network (DUMA), and Explainable Multi-Channel Generative Detector (EMC-GAN) were introduced. Each model predicted the future trend of sensor changes under the same input conditions. The predicted curves were compared with the actual monitoring values, with a focus on observing the response shifts during abnormal periods before and after a fire. This comprehensive evaluation assessed the trend prediction accuracy and abnormal warning capabilities of each method. The results are shown in Figure 10.

In Figure 10(a), GAT-ConvPred showed noticeable drift in later fluctuation segments and larger residuals overall (MAE±SD: 0.245 ± 0.018), suggesting limited responsiveness to higher-frequency anomalies. In Figure 10(b), DUMA could flag mutation points but exhibited a smooth lag of several time steps, leading to under-fitting of complex transient changes (0.221 ± 0.014). In Figure 10(c), EMC-GAN reduced the average error compared with the previous two models (0.208 ± 0.013) but the prediction curve presented visible jitter and amplified noise responses, indicating weaker modeling of non-stationary patterns. In Figure 10(d), RV-GAN closely followed the true trajectory across fluctuation segments (0.176±0.011) and achieved a statistically significant improvement over the strongest baseline (EMC-GAN), $p < 0.05$ (paired t-test). These results confirmed that the proposed two-stage design provided more stable and accurate predictions, particularly for transient and non-stationary dynamics.

To verify the adaptability and deployment scalability of the model in sensor networks of different sizes, the experimental setup simulated three network configuration scenarios with 10, 20, and 40 sensor nodes, respectively, to comprehensively evaluate the detection performance and deployment cost of the model. The results are shown in Table 3.

Table 3: Performance comparison under different sensor network scales.

Number of nodes	Model	False alarm rate (%)	Anomaly recall (%)	Computational complexity (GFLOPs)	Model parameters (M)	Inference time (ms)	Runtime memory (MB)	Average power (W)
10	GAT-ConvPred	7.1	86.4	2.3	3.6	13.7	112	4.6
	DUMA	6.3	88.7	3.1	5.0	15.9	128	5.2
	EMC-GAN	5.9	90.2	4.5	6.3	18.5	145	5.9
	RV-GAN	4.2	93.6	5.2	7.8	20.2	162	6.3
20	GAT-ConvPred	8.0	85.7	2.7	3.6	14.3	115	4.8
	DUMA	6.6	87.9	3.4	5.0	16.6	132	5.3
	EMC-GAN	6.1	89.4	4.9	6.3	19.3	149	6
	RV-GAN	4.9	92.7	5.6	7.8	21.0	166	6.4
40	GAT-ConvPred	8.7	84.1	3.4	3.6	15.2	120	5
	DUMA	7.2	86.5	3.9	5.0	17.3	136	5.5
	EMC-GAN	6.7	88.0	5.3	6.3	20.5	153	6.2
	RV-GAN	5.4	91.2	6.1	7.8	22.4	170	6.5

As shown in Table 3, RV-GAN consistently maintains excellent performance across various network scales, demonstrating good model stability and scalability. Taking a 40-node scenario as an example, RV-GAN achieves a false alarm rate of 5.4% and an anomaly recall rate of 91.2%. Although RV-GAN's computational complexity is 6.1 GFLOPs, its model parameter size reaches 7.8M, and its inference time is 22.4 ms, slightly higher than other methods, its detection accuracy is significantly superior. Furthermore, RV-GAN's average memory usage was 162-170 MB and its average power consumption was 6.3-6.5 W across various node scales. While its resource consumption was slightly higher than that of the lightweight GAT-ConvPred model, its inference time was consistently under 25 ms, meeting the real-time requirements of ultra-high-rise fire monitoring systems. This demonstrated that the proposed model stroke a good balance between detection accuracy and deployment cost.

4 Discussion

To enhance anomaly recognition accuracy and robustness in complex monitoring environments, this study proposed a two-stage anomaly detection model, CRSP-Pre + RV-GAN, combining low-rank completion and generative adversarial learning. Compared with the DUMA model [11], which relied mainly on global

attention and struggles to capture local fluctuations, the proposed RV-GAN introduced a residual temporal convolution structure that strengthened local dynamic response while maintaining global correlation, leading to improved reconstruction stability under high missing rates. When the number of nodes was 40, RV-GAN achieved a false alarm rate of 5.4% and a recall of 91.2%, outperforming DUMA by 4–5 percentage points in accuracy and stability. Compared with the lightweight wavelet–vector clustering method by Ahmad et al. [8], which attained 93.2% accuracy on drift readings but showed limited adaptability to multi-dimensional coupling and data loss, the proposed CRSP-Pre achieved structured data repair through correlation constraints and Schatten-p low-rank optimization. At a 50% missing rate, its MAE and SSIM surpassed those of single-stage completion models, confirming the framework's robustness in complex building environments.

The superiority of RV-GAN mainly stemmed from three factors: (1) the variational latent-space mechanism preserved multi-scale correlated features, improving anomaly separability; (2) the residual temporal convolution balanced local sensitivity and global consistency, reducing oversmoothing; and (3) the Wasserstein-regularized discriminator enhanced training stability and prevented mode collapse. The model introduced only moderate computational overhead—7.8M parameters and an 8% increase in GFLOPs compared to EMC-GAN—while maintaining an inference latency of 22.4 ms, satisfying real-time requirements.

From a control perspective, the framework exhibited adaptive and robust characteristics similar to classical fuzzy, neural adaptive, and backstepping control methods by dynamically reconstructing corrupted inputs and maintaining detection stability under uncertainty. In practical deployment, its computational complexity grew approximately linearly with sensor count and could sustain real-time performance on edge gateways with at least 1 GB of memory. The model was compatible with heterogeneous sensor types (smoke, temperature, infrared, CO), though large-scale synchronization and calibration remain engineering challenges for future implementation.

5 Conclusion

In summary, the proposed CRSP-Pre + RV-GAN model effectively enhanced the recognition accuracy and robustness of anomalous sensor data in super high-rise fire monitoring systems. By integrating structured data restoration and adversarial high-order anomaly detection, the model achieved stable processing of multi-source, high-missing data and demonstrated clear advantages over existing methods. The dual-module framework thus exhibited strong data adaptability and high detection precision, meeting the anomaly monitoring requirements of large-scale sensor networks in complex building environments.

However, some limitations remain. The model's computational complexity and parameter size constrained its deployment on lightweight edge devices. With approximately 7.8 M parameters, the weight memory was around 31 MB (FP32) or 15 MB (FP16), and the estimated runtime footprint reached 160–180 MB, exceeding the memory budgets of microcontroller-class hardware but remaining feasible for edge gateways or SoC platforms with ≥512 MB RAM. Moreover, the method primarily relied on training with known anomaly types, leaving room for improving generalization to unseen patterns. Future research may focus on lightweight structure optimization, quantization, and multi-modal transfer learning to enhance adaptability and robustness under multi-source complex scenarios.

References

[1] Tanaka K, Kudo M, Kimura K. Sensor data simulation for anomaly detection of the elderly living alone. IEEE Internet of Things Journal, 2024, 11(19):31675-31686. DOI:10.1109/JIOT.2024.3421548

[2] Rigatos G, Abbaszadeh M, Sari B, Siano P, Cuccurullo G, Zouari F. Nonlinear optimal control for a gas compressor driven by an induction motor. Results in Control and Optimization, 2023, 11: 100226. DOI: 10.1016/j.rico.2023.100226

[3] Boulkroune A, Zouari F, Boubellouta A. Adaptive fuzzy control for practical fixed-time synchronization of fractional-order chaotic systems. Journal of Vibration and Control, 2025: 10775463251320258. DOI: 10.1177/10775463251320258

[4] Wang S, Weng W. Dilemmas and directions of real-time detecting trapped individuals using ultra-wideband radar in building fire rescue. Frequenz, 2023, 77(9): 425-442. DOI:10.1515/freq-2022-0237

[5] Jana S, Shome S K. Hybrid ensemble-based machine learning for smart building fire detection using multi modal sensor data. Fire Technology, 2023, 59(2): 473-496. DOI:10.1007/s10694-022-01347-7

[6] Gursel E, Reddy B, Daniels K, Coble J B, Madadi M, Agarwal V, Khojandi A. SPIDARman: System-level physics-informed detection of anomalies in reactor collected data considering human errors. Nuclear Technology, 2024, 210(12): 2299-2311. DOI:10.1080/00295450.2024.2338507

[7] Wang Z, Gao R, Gao C, Chen Y, Wang F. A Distributed anomaly detection scheme based on correlation awareness in WSN. Wireless Personal Communications, 2024, 134(1): 519-541. DOI:10.1007/s11277-024-10930-w

[8] Ahmad R, Alhasan W, Wazirali R, Almajalid R. A Reliable approach for lightweight anomaly detection in sensors using continuous wavelet transform and vector clustering. IEEE Sensors Journal, 2024, 24(15):24921-24930. DOI:10.1109/JSEN.2024.3407158

[9] Su Y, Ma J, Fan J, Chen B, Zhou J, Yin B. A WSN data stream anomaly detection algorithm based on GATv2-TCN joint optimization. Computer Engineering & Science, 2025, 47(5): 843-850. DOI:10.3969/j.issn.1007-130X.2025.05.008

[10] Allka X, Ferrer-Cid P, Barcelo-Ordinas J M, Garcia-Vidal J. Leveraging spatiotemporal correlations with recurrent autoencoders for sensor anomaly detection. IEEE Internet of Things Journal, 2024, 11(19):31144-31152. DOI:10.1109/JIOT.2024.3416525

[11] Pan J, Ji W, Zhong B, Wang P, Wang X, Chen J. DUMA: Dual mask for multivariate time series anomaly detection. IEEE Sensors Journal, 2022, 23(3): 2433-2442. DOI:10.1109/JSEN.2022.3225338

[12] Gutierrez-Rojas D, Kalalas C, Christou I, Almeida G, Eldeeb E, Bakri S, Nardelli P H. Detection and classification of anomalies in WSN-enabled cyber-physical systems. IEEE Sensors Journal, 2024, 25(4):7193-7204. DOI:10.1109/JSEN.2024.3520507

[13] Prabowo O M, Supangkat S H, Mulyana E, Nugraha I G B B. Improving internet of things platform with anomaly detection for environmental sensor data. International Journal of Advanced Computer Science and Applications, 2022, 13(8):208-214. DOI:10.14569/IJACSA.2022.0130825

[14] Boulkroune A, Hamel S, Zouari F, Boukabou A, Ibeas A. Output-feedback controller based projective lag‐synchronization of uncertain chaotic systems in the presence of input nonlinearities. Mathematical Problems in Engineering, 2017, 2017(1): 8045803. DOI: 10.1155/2017/8045803

[15] Lu C, Tang J, Yan S, Lin Z. Nonconvex nonsmooth low rank minimization via iteratively reweighted nuclear norm. IEEE Transactions on Image Processing, 2015, 25(2): 829-839. DOI: 10.1109/TIP.2015.2511584

[16] Zouari F, Saad K B, Benrejeb M. Robust neural adaptive control for a class of uncertain nonlinear complex dynamical multivariable systems. International Review on Modelling and Simulations, 2012, 5(5): 2075-2103. DOI: 10.1016/j.neucom.2012.09.036

[17] Suklabaidya S, Das I. Comparative exploration of CNN model and transfer learning on fire image dataset. Innovations in Systems and Software Engineering, 2022, 21(1):247-256. DOI:10.1007/s11334-022-00521-y

[18] Zouari F, Saad K B, Benrejeb M. Adaptive backstepping control for a class of uncertain single input single output nonlinear systems. 10th International Multi-Conferences on Systems, Signals & Devices 2013 (SSD13). IEEE, 2013, pp. 1-6. DOI: 10.1109/SSD.2013.6564134

[19] Prabowo U N, Saroji S, Sismanto S. Geophysical-guided Wasserstein cycle-consistent generative adversarial networks for seismic impedance inversion. Acta Geophysica, 2025, 73(3):2621-2634. DOI:10.1007/s11600-025-01536-2

[20] Zouari F, Saad K B, Benrejeb M. Adaptive backstepping control for a single-link flexible robot manipulator driven DC motor. 2013 International Conference on Control, Decision and Information Technologies (CoDIT). IEEE, 2013, 864-871. DOI: 10.1109/CoDIT.2013.6689656